Identifying Cu-oxo species in Cu-zeolites by XAS: A theoretical survey by DFT-assisted XANES simulation and EXAFS wavelet transform

(Article begins on next page)

20 April 2024

Identifying Cu-oxo species in Cu-zeolites by XAS: a theoretical survey by DFT-assisted XANES simulation and EXAFS wavelet transform

Ilia A. Pankin[1,2], Andrea Martini[1,3], Kirill A. Lomachenko[4], Alexander V. Soldatov[1], Silvia Bordiga[2,5], Elisa Borfecchia[2]*

Dedicated to Prof. Carlo Lamberti

[1]*Smart Materials, Research Institute, Southern Federal University, Sladkova Street 174/28, 344090 Rostov-on-Don, Russia.*
[2]*Department of Chemistry, CrisDi Interdepartmental Center, University of Turin, via P. Giuria 5, 10125 Turin, Italy.*
[3]*Department of Physics, CrisDi Interdepartmental Center, University of Turin, via P. Giuria 1, 10125 Turin, Italy.*
[4]*European Synchrotron Radiation Facility, 71 avenue des Martyrs, CS 40220, 38043 Grenoble Cedex 9, France.*
[5]*Center for Materials Science and Nanotechnology (SMN), Department of Chemistry, University of Oslo, 1033 Blindern, 0315 Oslo, Norway.*

(*) Corresponding Author: elisa.borfecchia@unito.it

Keywords

Abstract

Cu-exchanged zeolites are attracting increasing attention as platforms for high-impact selective redox chemistry, including NH_3-mediated selective catalytic reduction of harmful nitrogen oxides (NH_3-SCR) and selective oxidation of methane to methanol (MTM). X-ray absorption spectroscopy (XAS) today represents a well-established and widespread technique for the characterization of these systems, but open challenges remain to accurately determine nuclearity and chemical identity of Cu-oxo species stabilized under high-temperature oxidative conditions. To systematically assess limitations and potential of XAS in this context, here we consistently explored by DFT a set of monomeric and dimeric Cu^{II} species incorporated in the chabazite (CHA) and mordenite (MOR) frameworks, envisaged as key players for both NH_3-SCR and MTM. We present a combined DFT-assisted analysis based on both full-potential XANES simulation and Wavelet Transform Analysis (WTA) applied to computed EXAFS signals. The resulting theoretical insights set the bases for an easier and more robust interpretation of the XAS data collected on Cu-zeolite systems. In particular, we evidenced possible fingerprint features in the XANES region, together with the difficulties in discriminating among monomeric and dimeric Cu^{II} moieties solely based on their XANES signatures. We then show the potential of Wavelet Transform Analysis as a new tool in the identification and visualization of EXAFS atomic contributions, to possibly enhance the EXAFS sensitivity to the nuclearity of Cu-oxo species in Cu-zeolites.

1. Introduction

Zeolites are extensively used in heterogeneous catalysis as their inner cavities offer a confined environment providing high selectivity for a wide range of reactions [1]. Among them, Cu-exchanged zeolites are efficient catalysts that have shown promising performance for high-impact selective redox processes [2]. Cu-CHA, due to its excellent activity in a broad temperature range and superior hydrothermal stability, today represents the catalyst of choice for commercial $deNO_x$ applications in the automotive sector via ammonia-mediated selective catalytic reduction (NH_3-SCR) [2-4]. More

recently, a number of Cu-zeolites, have been shown to be active towards the selective oxidation of methane to methanol (MTM) [2, 5-8]. Although nature does the work masterfully with Cu-enzymes [9], an industrially-viable process for the MTM conversion remains a *holy grail* in chemistry [7]. Nonetheless, Cu-exchanged zeolites, including chabazite (CHA) [10, 11] and mordenite (MOR) [12-15], have been demonstrated to possess Cu-oxo active sites able to cleave the C−H bond of methane at temperatures ≤ 200 °C, enabling its stoichiometric transformation into methanol. Clearly, to understand the reliability and the potential of these material towards the MTM process, it is crucial to accurately characterize Cu-speciation during O_2 activation, when Cu active sites are formed. A detailed assessment of chemical identity and nuclearity of Cu-species formed under oxidative conditions at high temperature is also essential in the context of NH_3-SCR, especially for temperatures ≥ 250 °C, when Cu ions mostly occurs as framework-coordinated moieties [16]. To this end, X-ray absorption spectroscopy (XAS) is an established powerful tool, and it has been largely used to characterize Cu-zeolites under *in situ* or *operando* conditions in the activated state [17-19], during SCR [16, 20-23] and MTM reactions [11, 12, 14, 15, 24], as well as during interaction with selected reactants relevant to such chemistries [25-28]. The main reason lies in the local sensitivity of this technique and in its element selectivity, together with the possibility to simultaneously access both electronic and structural information [29-31]. However, the nature and nuclearity of Cu species in Cu-CHA and Cu-MOR, formed as a function of the zeolite topology and composition, is still hotly debated.

Experimental XAS data for Cu-CHA and Cu-MOR demonstrated that there is no sharp spectroscopic contrast in the O_2-activated state for the two topologies, neither in the XANES nor in the EXAFS region, once samples with equivalent Si/Al and Cu/Al ratios are considered [32] (see also Section 3.4). Moreover, the behavior of these two Cu-zeolites along the stepwise MTM process, as probed by operando XAS, is rather similar [32]. Nonetheless, the structural models adopted for quantitative analysis of the related EXAFS spectra significantly differs for the two topologies. While the first peak of the magnitude of the EXAFS Fourier Transform (FT) is fully recognized to be associated to Cu−O single scattering path (SS), the interpretation of the well-defined second-shell peak, most often observed in O_2-activated samples, appears to be more uncertain. In particular, this feature in Cu-CHA has been associated to the single scattering (SS) paths involving the second-shell Al/Si atoms in monomeric Cu-complexes [11, 18, 33]. Conversely, for Cu-MOR, the second-shell region is often modelled solely by the Cu−Cu SS paths characteristic of multimeric Cu species [12, 14].

In our endeavor to assess limits and potential of the XAS technique applied to the characterization of O_2-activated Cu-zeolites, herein we report a theoretical screening of the simulated XAS signals – in both XANES and EXAFS region – for a number of DFT-optimized Cu^{II}-oxo species hosted in the CHA and MOR zeolites. The characteristic Cu K-edge XANES features identified for three- and four-fold coordinated species represent a useful tool to aid the analysis of the experimental XANES spectra. At the same time, the reported results highlight the difficulties of conventional XANES in discriminating mono- and dicopper(II) species retaining the same trigonal coordination motif for the Cu^{II} ions.

To underline the high level of complexity associated to the interpretation of the EXAFS-FT in the second-shell region for Cu-CHA and Cu-MOR, even in the ideal *single-species* case accessed by theory, we analyze the different SS contributions in computed EXAFS spectra for representative mono- and di-copper species in the two zeolites. Wavelet Transform Analysis (WTA) [34-38] is finally presented as a promising approach to enhance the EXAFS sensitivity to the nuclearity of Cu-

species in zeolites, representing an ongoing challenge for XAS with profound implications for both MTM and SCR chemistries.

2. Methods

2.1. DFT details

Spin-polarized DFT simulations were performed using plane wave pseudopotential approach implemented in the VASP 5.3 package [39]. Cell volume, cell shape and atomic positions were used as variable parameters in the geometry relaxation procedure. Block Davidson scheme was employed for electronic SCF cycles calculations. A kinetic energy cutoff of 450 eV and 400 eV was used to restrict plane wave basis set for single point calculations and for cell shape and atomic positions relaxation, respectively. 3x3x3 and 2x2x6 K-point meshes automatically generated by means of Monokhorts-Pack scheme were implemented for sampling of Brillouin zone for volume optimization calculation of CHA and MOR topologies, respectively. Reduced 2x2x2 and 1x1x3 K-points meshes and density functional theory with the PBE functional [40] were employed for cell shape and atomic position relaxations to decrease the computational costs. DFT-D3 scheme by Grimme et al. [41] as implemented in VASP 5.3 has been employed to account for Van der Waals interactions.

Foremost, for each model of CHA and MOR topologies, unit cell volume optimizations were carried out keeping cell shape and atomic positions fixed. The volume optimization has been performed by a set of single point calculations using a scaling coefficient aimed to mimic isotropic stretching/compressions (see Supplementary Material, Table S1). The cell shape and atomic positions were relaxed keeping the optimized value of the unit cell volume. In all geometry optimization runs, atomic positions were relaxed until the energy threshold of 1×10^{-6} eV was fulfilled. In a subsequent step total energy was estimated for the fixed geometries using the HSE06 functional [42].

To estimate the relative stabilities of different monomeric and dimeric species hosted in CHA and MOR framework we have calculated the chemical potential of the Cu atoms (μ^{Cu}) following the approached proposed by Ipek et al. [10], for the Cu geometries of different nuclearity:

$$\mu^{Cu} = \frac{1}{x}\left(G^{Cu_xO_yH_z+zeo} - G^{2H+zeo} - \frac{z-x}{2}\mu^{H_2O} - \frac{2y-z+2x}{4}\mu^{O_2}\right) \quad (1)$$

where G is the corresponding Gibbs free energy, approximated as the sum of the DFT-computed electronic energy of the system and the corresponding zero point energy contributions (ZPE), neglecting the entropy term and μ^{H_2O} and μ^{O_2} are the corresponding chemical potentials (see Supplementary Material for details). For each model as well as for the protonic form of the investigated zeolites, vibrational frequency calculations have been performed by using finite difference method as implemented in VASP [39] with an atomic displacement equal to 0.015 Å. For frequency calculation Brillouin zone sampling was restricted to the Γ point.

2.2. XANES simulations

Finite difference method in a full potential approximation as implemented in FDMNES code [43] was employed to simulate Cu K-edge XANES spectra for different Cu-oxo species hosted in both CHA and MOR frameworks. The code is originally representing a monoelectronic approach and is fully relativistic. Thus, it is able to account for spin-orbit coupling in both the core state and optionally in the final states. The *ab initio* calculations are carried out in the real space using clusters built around each nonequivalent absorber. The code is based on the *ab initio* calculations of the electronic structure first, and further solving of the Schrödinger equation (discretized radial Schrödinger equation when

the finite difference method approach is used) in the finite number of the grid points in a real space grid where the atomic potential is determined by superposing the self-consistent atomic potentials [44]. The energy-dependent exchange-correlation potential is evaluated using local density approximation (LDA) relying on Hedin-Lunquist formulation [45].

Sparse solvers for the finite difference matrix were used in order to decrease the required computational time [46]. To take into account the spectra convolution due to the finite life-time of the Cu *1s* core hole, corresponding convolution parameters have been set up in accordance to the tabulated value of 1.55 eV [47].

In the present work, XANES spectra has been calculated for an atomic cluster with a size determined by a 7 Å radius centered in the absorbing atom (see also Figure S6 and S7 of Supplementary Material). The position of Fermi level has been estimated for a non-excited system within a cluster of smaller radius set at 3.5 Å. Since the Fermi level energy varies in the ± 0.5 eV range for different models, to have the same convolution parameters for all geometries the average value of Fermi energy was used. For di-copper species, the final spectra were obtained by averaging over the two independent calculations for different inequivalent Cu sites.

2.3. Wavelet Transform Analysis on EXAFS spectra

Wavelet Transform Analysis (WTA) is a powerful technique, inherited from the signal processing field, that is attracting a great interest in the XAS community, especially for the identification of the overlapped contributions coming from different neighbor atoms or scattering events (i.e. single or multiple scattering) [34-37]. If two or more groups of different atoms are localized at close distances around the absorber, their contributions in the direct space R overlap, becoming indistinguishable. This makes the classical FT analysis of the EXAFS spectrum rather uninformative [36]. However, from a detailed analysis of the EXAFS equation, it is possible to observe that the localization of the curved-wave harmonic contributions, coming from the different scatterers which surround the absorbing atom, are localized in the k-space, principally thanks to the backscattering amplitude factor $F(k)$ [38]. This term is characterized by a strong dependence on the atomic number Z. In particular, heavy atoms, having large values of $F(k)$, are localized at higher wavenumbers than lighter atoms (and *vice versa*), see Figure 1. This evidence can be exploited by WTA for a finer signal discrimination allowing a two-dimensional representation of the EXAFS spectrum with a simultaneous signal localization in k and R space.

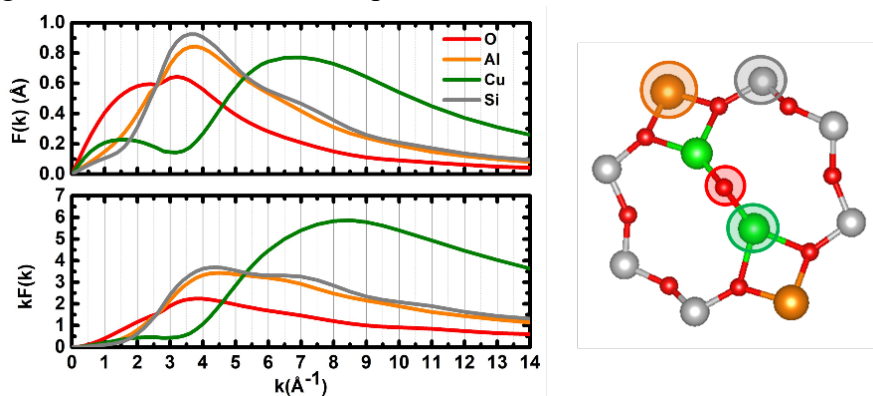**Figure 1.** Plot of the backscattering amplitude factor, k^0- (top) and k-weighted (bottom), calculated for the SS paths involving the Cu absorber and the circled atoms for a representative dicopper(II) species hosted in a zeolitic framework, namely ZCu^{II}O$^{\mu}$Cu^{II}Z in the CHA 8MR, geometry shown on the right. Atom color code as follows: Cu, green; O, red; Si, grey; Al, orange.

The Wavelet Transform (WT) of a general k^n-weighted EXAFS spectrum is described by the following two-dimensional integral transform:

$$w(a,b) = \frac{1}{\sqrt{a}} \int_{-\infty}^{+\infty} k'^n \chi(k') \psi^* \left(\frac{k'-b}{a}\right) dk' \tag{2}$$

This equation can be seen as the inner product between the k^n-weighted EXAFS spectrum $\chi(k)$ and a defined window function ψ, called "mother wavelet" or simply wavelet (where the apex ψ^* denotes the complex conjugate of ψ), which must decay at zero for higher values of $|k'|$ [35]. Here, the signal $\chi(k)$ is analysed through a set of train-waves (wavelets) that are shifted by b units in the k-space and distorted by a factor a in order to take account of the local frequencies of the signal [38]. The variables a and b are connected to k- and R-space by the following relations: $b = k$ and $a = \eta/2R$, where η is a parameter that depends on the window function used, regulating the signal resolution in the k and R spaces. For this reason, the selection of an appropriate η value is critical. It is worth mentioning that the WT distributes the signal information over some k-R cells usually referred to as *uncertainty* or *Heisenberg boxes* [37]. On this basis, it is possible to demonstrate that the resolution in k and R space are inversely proportional; this means that a good resolution in k-space always implies a loss of information in the R-space, and vice versa. In our work, we chose as window function the Cauchy wavelet [34], represented by the following expression:

$$\psi(k) = \left(\frac{i}{k+i}\right)^{\eta+1} \tag{3}$$

Where i denotes the complex unit. We focused on this function because of its ability to simplify equation (2). Moreover, the usage of a complex-valued function seems to be more suitable for analyzing frequency-modulated signals [34]. Indeed, through eq. (3), the signal resolution is controlled by just one parameter (i.e. η) instead of additional terms, as in the case of other wavelet mother function such as the Morlet wavelet [35-37].

2.4. EXAFS simulations details

Focusing on the EXAFS simulations, for each Cu site in the CHA and MOR framework, we calculated the phases and amplitudes of each path using the FEFF 6.0 code implemented in the Artemis software from the Demeter package [48]. Herein, we based our simulations on the assumption, supported by experimental results [16, 18, 19], that in the R-space range of interest (up to 4 Å), SS paths represent the dominant contribution to the EXAFS signal. The structural parameters (*i.e.* coordination number N_i and bond distances R_i) for all the included coordination shells were set to the DFT values. The Debye Waller (DW) parameters have been chosen for each shell according to the types of atoms and their distances from the absorber. This was done on the basis of some recent experimental work conducted on this topic [11, 18]. We fixed, for the extra-framework oxygen (O_{efw}), the DW parameter to 0.005 Å^2 with the exception of the second extra-framework oxygen O_{efw_2} in the $ZCu^{II}O_2^{end}$ and $ZCu^{II}O_2^{end}Cu^{II}Z$ geometries where, in order to account for the higher disorder effect, the DW was fixed to 0.006 Å^2. The same value (0.005 Å^2) has been used to describe the contributions involving the second sub-shell of framework oxygens (O_{fw}). We set the DW factor related to the Al coordination shell to 0.008 Å^2. A 0.008 Å^2 DW value was also fixed for the second Cu site in di-copper species. For the farer O and Si framework atoms, which provide a minor but not

negligible contribution to the EXAFS signals, we employed a lower-level parametrization strategy. We assigned a DW factor defined in the following way: $\sigma^2 = \sigma_{fw}^2 \cdot \sqrt{R_i/R_Z}$, where σ_{fw}^2 has been fixed to a global value of 0.01 Å^2, R_i is the optimized distance from the Cu absorber for ith atom, while the term R_Z represents the distance of the nearest framework atom from the Cu absorber. This choice seems appropriate; in fact, it provides a slow increase of the DW factor as the distance increases (*i.e.* isotropic increasing), accounting for the structural or thermal disorder typically more pronounced at higher distances from the absorber [49]. Finally, we set the amplitude factor S$_0$ to 1 (ideal value) and the absorption edge energy shift to 0 eV. In case of di-copper sites, we observed that the local environments associated to the two Cu-absorbers are not fully equivalent (see Table S4 and Table S5 for detailed information about structural parameters): some small but not negligible differences appear. For this reason, initially, we considered each of the Cu atoms separately (i.e. one Cu atom has been set as the absorber while the second-one as the scattering atom) applying the parametrization described above for each Cu site. Afterwards, we merged the two simulated k^{2}χ(k) EXAFS signals in order to obtain a single common spectrum. Once that the set of theoretical EXAFS spectra were calculated, we processed them by WTA selecting for each structure a common parameter η set to 200, which allows the best compromise, in term of resolution, among the *k* and R spaces. In the following, for all the structures analyzed, the Fourier transforms of the EXAFS signals are phase-uncorrected and obtained transforming the simulated k^{2}χ(k) EXAFS signals in the 2.4-11.0 Å^{-1} range.

2.5 Experimental XAS data for comparison with theoretical results

The experimental XAS spectra reported in Section 3.4 for the sake of comparison with theoretical results have been collected on the BM26A beamline of the ESRF [50] on Cu-CHA and Cu-MOR with similar compositional characteristics (Cu-CHA: Cu/Al = 0.5; Si/Al = 12; Cu-MOR: Cu/Al = 0.4; Si/Al = 11) measured (i) after activation in O$_2$-flow at 500 °C and (ii) after cooling to 200 °C in O$_2$-flow and flushing with He, always at 200 °C. The data have been previously published in ref. [32]; the reader is referred to the original publication for additional details on sample synthesis, treatment, as well as details on XAS data acquisition strategy.

3. Results and discussion

3.1. Models description and DFT-results

Smaller rings in zeolite frameworks are believed to favor the coordination of Cu species [51], although the resulting Cu-sites may be less accessible for guest molecules to react. Conversely, larger rings enhance the diffusion of reactants and products and thus make the Cu active sites more exposed for catalysis. Focusing on Cu-oxo species possibly derived from molecular oxygen activation during high-temperature treatment [10, 15], in our structural screening we mostly considered the larger rings offered by the CHA and MOR topologies, in principle more accessible to O$_2$, also based on the detailed computational study by Vilella et al. [51]

Previous works [10, 11, 18, 33, 52, 53] have also shown that monomeric Cu^{II} species could be hosted at both 2Al sites in double 6MR and 1Al sites in 8MR of CHA framework, as redox-resistant bare Z$_2$Cu^{II} ions or ZCu^{II}OH moieties, respectively. Here, we focused on ZCu^{II}OH moieties, due to the possible involvement of these species in selective redox processes over both CHA and MOR.

In addition to ZCu^{II}OH, we also considered two super-oxo Cu^{II} moieties with four-fold coordinated side-on (ZCu^{II}O$_2$^{side}) and three-fold coordinated end-on (ZCu^{II}O$_2$^{end}) binding mode. With respect to dimeric Cu^{II} species, we investigated three-fold coordinated mono-(μ-oxo) cores ZCu^{II}O$^\mu$Cu^{II}Z and

ZCu^{II}O$_2$^{end}Cu^{II}Z peroxides, with end-on O$_2$ binding mode. For the CHA topology, based on previous theoretical investigation by Falsig et al. [52], we have computed the ZCu^{II}O$_2$^{end}Cu^{II}Z geometry locating the two Al atoms in adjacent 6MR and 8MR of the framework. In all the other cases, the Cu^{II} ions are located in the same zeolite ring – 8MR and 12MR for CHA and MOR, respectively – with Al···Al separation chosen on the basis of previous literature reports [51].

The overall selection of structures is also motivated by previous works [10, 11, 54-56] pointing to two possible routes to form Cu-oxo framework-coordinated species: (i) from a self-reduced ZCu^{I} by interaction with an oxygen molecule which can result to the formation of monomeric superoxo or dimeric peroxo species or (ii) due to internal pathways e.g. via condensation of proximal ZCu^{II}OH yielding to mono μ-oxo dicopper(II) cores. In both mechanisms, redox-active ZCu^{II}OH species represent a viable starting point [11], which also implies quite abundant population of this species in the activated samples. It is worth to emphasize that mixed-valence Cu^{II}/Cu^{III} trimers [14] and Cu^{III} dimers, *e.g.* bis (μ-oxo) di-copper (III) [12], also proposed in the literature, have not been considered here because of the lack of conclusive experimental evidences for Cu^{III} by XAS [57, 58].
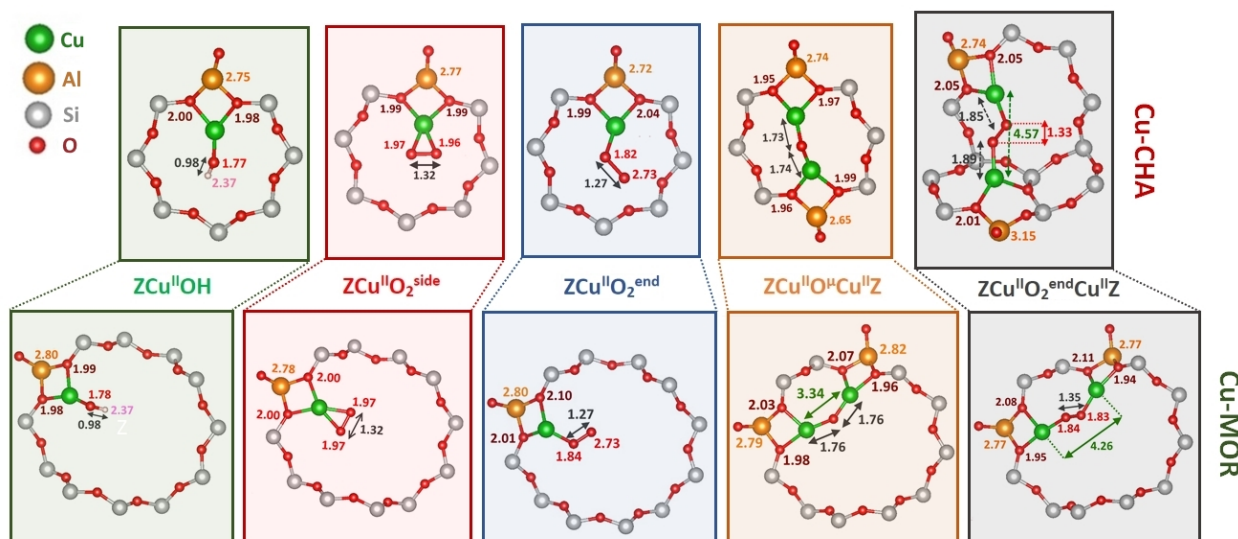

Figure 2. DFT-optimized geometries of different monomeric and dimeric Cu-oxo species incorporated into 8MR of CHA and 12MR of MOR frameworks (the rest of the zeolite framework is omitted for clarity). DFT-optimized interatomic distances are indicated in Å.

For each zeolite topology, Cu^{II} geometries have been incorporated into pre-optimized 36 T-sites unit cell of CHA and 48 T-sites unit cell of MOR and subsequently optimized taking into account as an initial guess structural parameters previously reported in the literature, using cluster [18, 19] and periodic [10, 51, 52] DFT-based approaches. The distribution of Al sites within zeolite framework is still hotly debated in the literature, and it has been proven to be strongly influenced by the synthesis conditions [59-62] In accordance with the previous DFT findings reported by Vilella and Studt [51], from the computational point of view there are no essentially inequivalent T-sites for Al hosting both in CHA and MOR topology. For dimeric Cu-oxo species, we considered configurations with 3 and 2 Si atoms between two Al docking sites, in accordance with previously reported models [51], yielding very similar Cu-Cu and Al-Al spacing after DFT relaxation (see Table S4 and S5 in Supplementary Material).

After preliminary atomic position relaxation, volume optimization has been also performed (see Table S1 in Supplementary Material). Considering the relatively small Cu-loading in Cu-exchanged zeolite samples (typically in the 1-3 wt% range), the presence of Cu should not significantly affect the lattice

parameters and the volume optimization step, in principle, could be ignored. Nevertheless, since XANES is known to be very sensitive even to small changes in bond lengths in proximity of absorbing atoms, we have considered a possible local perturbation in the unit cell volume when the Cu sites are included. To obtain the final geometry, a second step of atomic position relaxation has been performed, keeping the unit cell volume fixed to the optimized value. The results of DFT-optimization are summarized in Table 1, while the optimized geometry obtained for the selected Cu^{II}-oxo species are visualized in Figure 2. Additional illustrations of the final geometries (including all framework sites within the unit cell) as well as a detailed report on structural parameters can be found in the Supplementary Material, Figure S2, S3 and Table S4, S5, respectively.

Table 1. Averaged interatomic distances from Cu ions to framework (O_{fw}) and extra-framework (O_{ef}) oxygens as well as to charge-balancing aluminum sites and copper in Cu dimers. The relative values of μ^{Cu} are reported with respect to the most stable $ZCu^{II}O^{\mu}Cu^{II}Z$ models. The absolute values, together with details of all contributions to μ^{Cu}, are presented in Supplementary Material, Table S2 and S3.

Model	$<\text{Cu-O}_{ef}>$ (Å)		$<\text{Cu-O}_{fw}>$ (Å)		$<\text{Cu-Al}>$ (Å)		Cu-Cu (Å)		μ^{Cu} (kJ/mol)	
	CHA	MOR	CHA	MOR	CHA	MOR	CHA	MOR	CHA	MOR
$ZCu^{II}O_2^{side}$	1.97	1.97	1.99	2.00	2.77	2.78	-	-	78.46	67.44
$ZCu^{II}O_2^{end}$	1.82	1.84	2.00	2.06	2.73	2.80	-	-	97.92	76.12
$ZCu^{II}OH$	1.77	1.77	1.98	1.98	2.79	2.80	-	-	47.80	48.23
$ZCu^{II}O^{\mu}Cu^{II}Z$	1.74	1.77	1.96	2.02	2.70	2.80	3.06	3.34	0.00	0.00
$ZCu^{II}O_2^{end}Cu^{II}Z$	1.87*	1.83*	2.10	1.95	2.95	2.77	4.57	4.26	33.55	20.91

* To obtain an averaged $Cu-O_{ef}$ for $ZCu^{II}O_2^{end}Cu^{II}Z$ models only nearest extra-framework oxygen to each Cu sites was accounted.

In accordance with previously published DFT results obtained within PAW-PBE level of theory [10, 33, 51, 63, 64], the two dimeric mono-(μ-oxo) $ZCu^{II}O^{\mu}Cu^{II}Z$ and peroxide $ZCu^{II}O_2^{end}Cu^{II}Z$ cores are among the most stable species, followed by monomeric $ZCu^{II}OH$. A small discrepancy in the relative stability of the two dicopper(II) geometries with respect to the findings reported by Ipek et al. [10] could be caused by different Al⋯Al separation chosen for mono-(μ-oxo) dimers (3Si in this work and 2Si for geometry reported by Ipek [10]) and slightly different DFT parameters (e.g. Brillouin zone sampling). The decrease of μ^{Cu} obtained for $ZCu^{II}O_2^{end}Cu^{II}Z$ in MOR with respect to CHA is in line with findings by Vilella et al. [51], indicating that peroxo dicopper(II) species are more stable for zeolites consisting of 10MR and 12MR (such as MOR and MFI) providing Al⋯Al spacing of ∼ 8Å.

The analysis of the averaged interatomic distances in the proximity of Cu ions demonstrates that for the same species incorporated into different zeolites topologies, the Cu local environment does not vary significantly. In some cases, almost the same bond lengths are observed, e.g. for $ZCu^{II}OH$ model the $Cu-O_{ef}$ and $Cu-O_{fw}$ distances in CHA and MOR frameworks are pretty much the same. These distances are also in perfect correspondence with the ones previously reported [18, 33, 63] for $ZCu^{II}OH$ geometry hosted in 6MR and 8MR of CHA. For $ZCu^{II}O_2^{side}$ $Cu-O_{ef}$ and $Cu-O_{fw}$ distances are also very similar, optimized to 1.97 Å and 1.99 Å vs 1.97 Å and 2.00 Å for CHA and MOR, respectively. Relatively larger differences are observed for $Cu-O_{fw}$ distances only in dimeric models as well as for $Cu-Al$ distances comparing different species incorporated into the same framework and the same species incorporated into different frameworks. The similarity of the DFT optimized distances obtained for the same species hosted in the CHA 8MR and MOR 12MR of MOR, together with the very similar distances obtained for superoxo species considered in 6MR of CHA by McEwen

[63], implies only a minor effect from the framework environment. Table 2 reports the computed electronic properties of Cu ions in the considered models.

Table 2. Summary of DFT calculated spin state, magnetic moments and normalized charges of Cu ions.

Model	Spin state		Cu charge*		Cu magnetic moment	
	CHA	MOR	CHA	MOR	CHA	MOR
$ZCu^{II}O_2^{side}$	Triplet		2.04	2.03	0.428	0.428
$ZCu^{II}O_2^{end}$	Triplet		1.88	1.90	0.347	0.359
$ZCu^{II}OH$	Doublet		2.02	2.02	0.513	0.521
$ZCu^{II}O^{\mu}Cu^{II}Z$	Singlet	Triplet	2.02	2.07	0.005	0.527
$ZCu^{II}O_2^{end}Cu^{II}Z$	Triplet		1.95	1.95	0.364	0.387

* The charge state has been calculated by means Bader analysis using Cu^I_2O and $Cu^{II}O$ oxides as refence compounds for charge normalization. Charges and magnetic moments for dimeric species obtained by averaging over two Cu ions.

For super-oxo models considered both in CHA and MOR the local minima energy geometries correspond to a triplet spin state having two unpaired e^- (multiplicity 3) shared between copper and the two extra-framework oxygens. This result falls in line with magnetic structure for super-oxo species hosted in 6MR of CHA reported by McEwen [63], where $ZCu^{II}O_2^{side}$.geometry has been found also to have doublet structure for a model with significantly shortened $Cu-O_{ef}$ distances. The $ZCu^{II}OH$, also adopting a three-fold coordinated conformation, appears to be relaxed in doublet spin state. Conversely, $ZCu^{II}O_2^{end}Cu^{II}Z$ exhibit triplet magnetic state in accordance with the recent results by Paolucci et al. for ammonia-solvated dicopper(II) peroxides with end-on O_2 binding mode [20]. The only Cu-species which demonstrates different magnetic behavior once incorporated in CHA or MOR is $ZCu^{II}O^{\mu}Cu^{II}Z$. It appears to be in singlet state in 8MR of CHA (having two unpaired e^- belonging to two different Cu sites with an opposite spin) while in the case of MOR it is in a triplet state (having two unpaired e^- with a parallel spin orientation).

Bader charge analysis confirmed that for all the geometries considered in this work the normalized charge of Cu ions is very close to the one obtained for $Cu^{II}O$ bulk oxide, namely equal to +2. However, there are some slight deviations from this "ideal" value, more pronounced for $ZCu^{II}O_2^{end}$ species in both CHA and MOR, resulting into a normalized charge equal to +1.882 and +1.901, respectively. Moreover, for most of the models, the normalized charge exhibits slightly higher values for the same species incorporated into MOR with respect to CHA. The only one exception to such trend is $ZCu^{II}O_2^{side}$ model, where we obtained for CHA framework a slightly higher normalized charge (+2.040) with respect to MOR (+2.028).

3.2. XANES simulations results

In spite of the huge potential of XANES theoretical analysis of local atomic and electronic structures of Cu species formed in Cu-zeolites, there are just a few works dealing with XANES simulations for these compounds. Recently, McEwen and coworkers have reported a systematic Cu K-edge XANES simulation study focusing on both framework-coordinated and water-/ammonia-solvated species in the cages of CHA zeolites [65]. In their earlier work, they also computed the theoretical XANES for bare Cu^I ions and various adsorbate-derived Cu-complexes in different locations within the CHA zeolite by using pseudopotential based CASTEP code [66]. Simulated XANES spectra for Cu sites in activated Cu-CHA were reported by Deka et al. [67], aiming to refine an XRD-based structural model. In our previous work we have also reported XANES simulation for bare ZCu^I, ZCu^{II} and $ZCu^{II}OH$ hosted in 8MR and 6MR of Cu-CHA within molecular orbitals approach [18, 19]. To the best of our knowledge, XANES spectra simulated for different framework-coordinated Cu^{II}-oxo

species within full potential finite difference method approach (see section 2.2) have not been reported previously.

Figure 3a reports the Cu K-edge XANES spectra simulated using the FDM approach for DFT-optimized monomeric and dimeric Cu-species in the CHA framework. The XANES spectrum simulated for the sole four-fold coordinated geometry, namely $ZCu^{II}O_2^{side}$, demonstrates a sharper difference with respect to the rest of the theoretical curves for the models considered in this work, exhibiting quite similar shape of the XANES. The XANES spectrum of $ZCu^{II}O_2^{side}$ is characterized by a well-defined white line (WL) peak (denoted as **C** in Figure 3a) and two less intense rising-edge shoulders (denoted as **A** and **B** in Figure 3a). Conversely, the theoretical spectrum stemming from $ZCu^{II}O_2^{end}$ shows less intense WL peak and more pronounced rising-edge peaks. The latter is also shifted towards higher energy. Another appreciable difference between the theoretical XANES for $ZCu^{II}O_2^{side}$ and $ZCu^{II}O_2^{end}$ is the energy positions of the WL peak, that is shifted towards higher energy in correspondence of end-on O_2 binding mode.

Overall, the shape of the theoretical XANES spectrum for $ZCu^{II}O_2^{end}$ is almost overlapped in the WL region with the spectra calculated for the other dimeric and monomeric Cu species, where the Cu^{II} centers are three-fold coordinated to two O_{fw} and one O_{ef} atom.
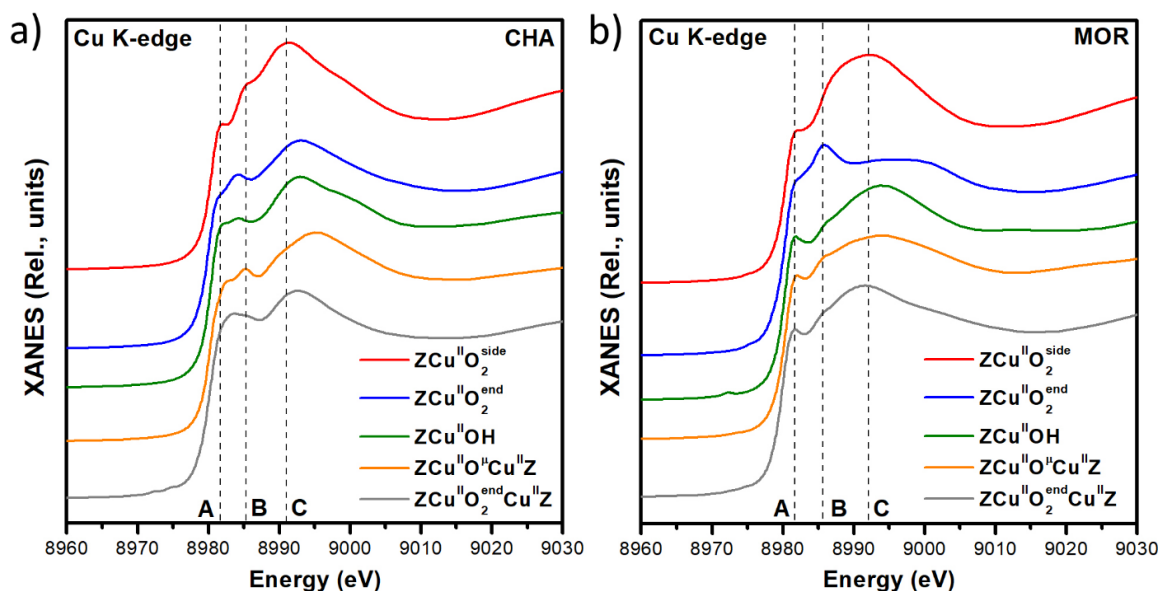

Figure 3. Cu K-edge XANES simulations for DFT-optimized Cu-oxo species in CHA (a) and MOR (b). Vertical dashed lines correspond to the energy position of the features **A**, **B** and **C** defined, for indication, based on $ZCu^{II}O_2^{side}$ model for CHA in part (a) and for $ZCu^{II}O_2^{end}Cu^{II}Z$ for MOR in part (b).

We only note subtle differences in the relative intensities of the **A** and **B** contributions in the rising-edge shoulder. In particular, for $ZCu^{II}O_2^{end}$ and $ZCu^{II}O^{\mu}Cu^{II}Z$, feature **B** is more pronounced with respect to the rest of three-fold coordinated geometries. Moreover, the theoretical spectrum obtained for $ZCu^{II}O^{\mu}Cu^{II}Z$ shows a slight shift to higher energy of the rising-edge feature **A** and significant shift of WL peak **C**, while retaining the same energy localization in the absorption edge region. There is also a clear trend in the energy distance between the absorption edge and WL peak **C** obtained for different Cu^{II} species, increasing as the $Cu–O_{ef}$ distance decreases, thus being minimum for $ZCu^{II}O_2^{side}$ ($<Cu–O_{ef}>$ = 1.97 Å) and maximum for $ZCu^{II}O^{\mu}Cu^{II}Z$ ($<Cu–O_{ef}>$ = 1.74 Å).

Similar trends can be emphasized also from qualitative analysis of the theoretical spectra for DFT-optimized monomeric and dimeric Cu-species hosted in 12MR of MOR, reported in Figure 3b. Again,

the spectrum simulated for four-fold coordinated $ZCu^{II}O_2^{side}$ exhibits larger differences with respect to all the other models, reflecting into higher intensity of WL peak **C** and lower intensity of rising-edge features **A** and **B**. It should be noted that in case of $ZCu^{II}O_2^{side}$ in MOR, feature **B** is not visible, being instead present in the spectrum of the same species in CHA. Also, feature **B** for $ZCu^{II}O_2^{end}$ is significantly more intense with respect to what it is observed for the other Cu-species in the MOR framework, being even more intensive than the WL peak itself. Such peculiar shape of the XANES spectrum computed for $ZCu^{II}O_2^{end}$ could be tentatively connected with a more pronounced lifting of the Cu-superoxo complex out from the 12MR plane, approaching the two oxygens in the adjacent 5MRs of MOR (see Figure S4 in Supplementary Material). This characteristic out-of-plane motion of the $ZCu^{II}O_2^{end}$ motif can also result in the smoother shape of WL peak **C** and in its shift to higher energy. For the others three-fold coordinated species incorporated into MOR framework, feature **B** appears to be less intensive and more convoluted with respect to the spectra simulated for the same moieties in CHA.

Overall, the observed differences in the shape of the XANES spectra computed for the geometry of the same Cu-species hosted in different framework − resulting into very similar DFT-optimized distances − highlight an appreciable effect of the distant framework environment on the simulated XANES.

In summary, XANES simulations by using FDM approach in full potential do not allow to highlight *nuclearity-sensitive* fingerprints in the spectra simulated for the selected monomeric and dimeric species incorporated into CHA and MOR topologies to conclusively discriminate between them. However, it is evident that in both cases, the larger differences were obtained for $ZCu^{II}O_2^{side}$ species, representative of four-fold coordinated Cu^{II} sites. Conversely, for the other three-fold coordinated monomeric and dimeric moieties, we do not observe pronounced differences. In all the cases, the computed curves show more intense rising-edge features and less developed WL peak with respect to $ZCu^{II}O_2^{side}$ with very similar XANES shape between the different three-fold coordinated models.

3.3. Wavelet Transform Analysis on simulated EXAFS spectra

Herein, we focus on the EXAFS signal stemming from two Cu^{II} species, namely $ZCu^{II}OH$ and $ZCu^{II}O^{\mu}Cu^{II}Z$, representative of Cu^{II} monomers and dimers in the CHA and MOR framework, often encountered in the literature related to both MTM and NH_3-SCR processes [2]. The two species are characterized by a similar, three-fold coordinated Cu local environment. As discussed in the previous section, they are difficulty discriminated solely based on their Cu K-edge XANES spectra.

We initially investigated the atomic contributions to the simulated conventional EXAFS-FT signal for the two species hosted in CHA and MOR. The results, reported in Figure 4, underpin the complexity related to the interpretation of the second-shell signal, due to the simultaneous presence of single scattering (SS) paths involving Al and Cu atomic neighbors, as well as the distant framework Si/O atoms. Moreover, the analysis of the magnitude and the imaginary part of each contribution provides deeper insights into the EXAFS-FT peaks assignment. The same simulated EXAFS spectra were further subjected to WTA, as illustrated in Figure 5, aiming to assess the potential of this alternative EXAFS analysis approach in discriminating among monomeric and dimeric Cu^{II} moieties.
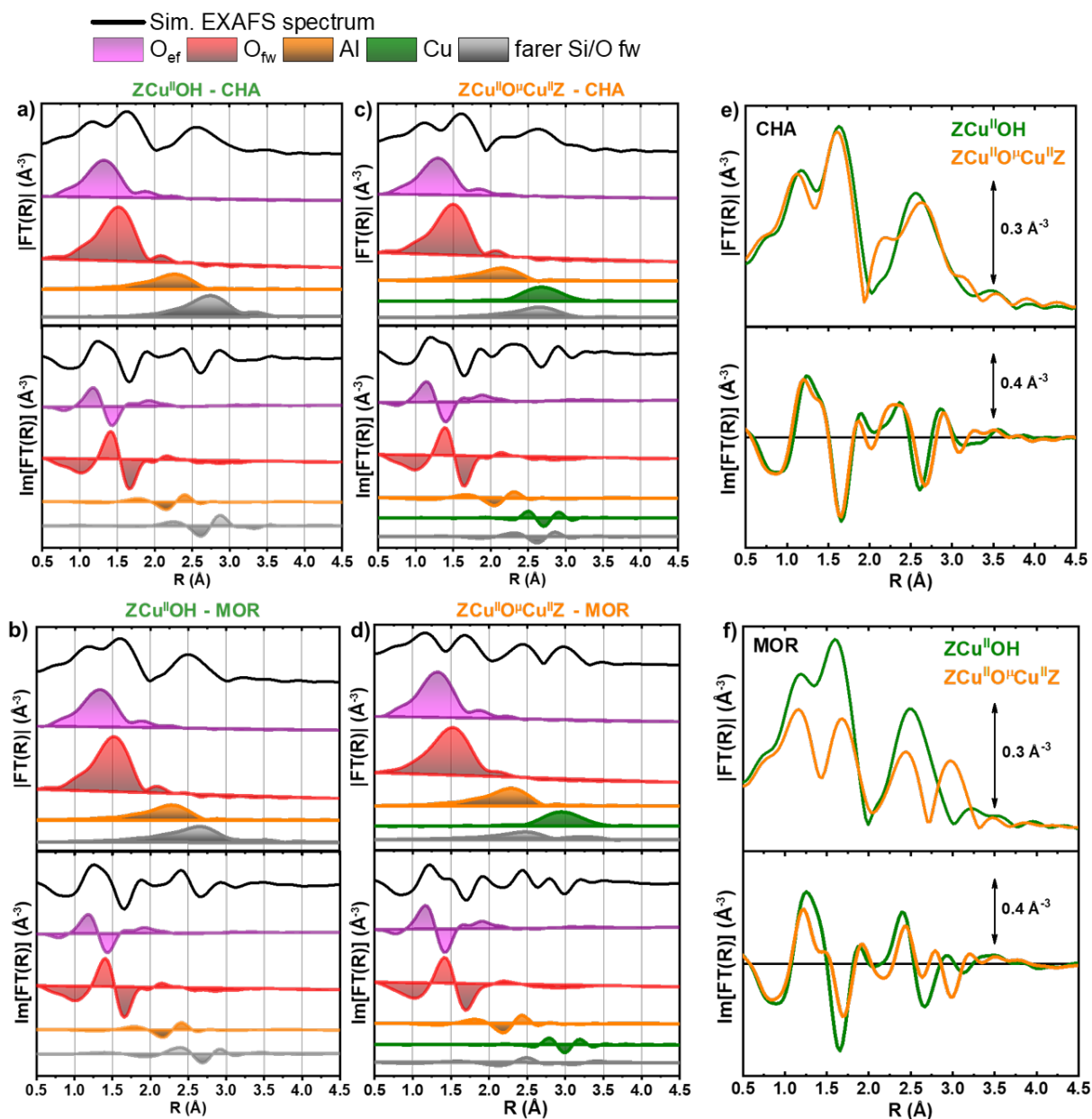
Figure 4. EXAFS-FT contributions of the simulated signals (magnitude: top panels, imaginary part: bottom panels) for ZCu^{II}OH monomers (CHA: (a); MOR: (b)) and ZCu^{II}O$^\mu$Cu^{II}Z dimers (CHA: (c); MOR: (d)), vertically translated for the sake of clarity. (e, f) Direct comparison between the magnitude (top panel) and the imaginary part (bottom panel) of the simulated EXAFS-FT for monomeric ZCu^{II}OH and dimeric ZCu^{II}O$^\mu$Cu^{II}Z species (e) in CHA and (f) in MOR. The selected range in k-space for all the EXAFS-FT spectra goes from 2.4 to 11.0 Å^{-1}. All the reported EXAFS-FT spectra are phase uncorrected.

Starting from monomeric ZCu^{II}OH structures, a common trend is evident for both the framework topologies, consistently with the high similarity between ZCu^{II}OH geometries in both CHA 8MR and MOR 12MR (see Table 1). ZCu^{II}OH results into a structured first-shell peak in the EXAFS-FT, where two sub-peaks are evident. The first sub-peak, less intense, is due to the O$_{efw}$ atom from the hydroxyl ligand, while the second one is related to the two nearest O$_{fw}$ atoms from the zeolite lattice, see Figure 4a,b. Scattering contributions stemming from Al and framework Si/O atoms are mostly in phase, thus promoting the growth of a well-defined second-shell peak at ca. 2.5 Å in the phase-uncorrected EXAFS-FT spectrum.

Considering the WTA results for ZCu^{II}OH, two main lobes are visible (Figure 5a,b). The first one, localized in the $\Delta R = (1.0–1.8)$ Å and $\Delta k = (0–12)$ Å^{-1} range, is associated to the O$_{fw}$ contributions,

with a sub-lobe, due to the O_{ef} atomic neighbor localized at lower R values. These features tend to be stretched in *k*-space towards higher *k*-values (around 12 Å^{-1}). Nevertheless, only atoms much heavier than oxygen should typically populate this region. The reason for this particular behavior represents a limitation of the analysis and it is due to the so-called *broadening effect*. It is a general problem of WTA, for low R-values, not only restricted to the Cauchy wavelet [36]. The second main lobe collects the contributions coming from the Al atom and the farer Si/O atoms from the zeolite lattice. It elongates till *ca.* 10 Å^{-1} because of the separate contributions coming from the Si and Al atoms from one side and the framework oxygens from the other, having a backscattering amplitude factor less intense at high *k*-values. It is worth noting that for all the analyzed cases, the spectral features related to the Si and Al atoms cannot be discriminated through WTA, because of their virtually equivalent backscattering amplitude factor (Figure 1). Always referring to Figure 1, it is clear that the contrast between O and Al/Si scatterers is rather limited, whereas for Cu scattering contributions, a better separation is in principle possible.
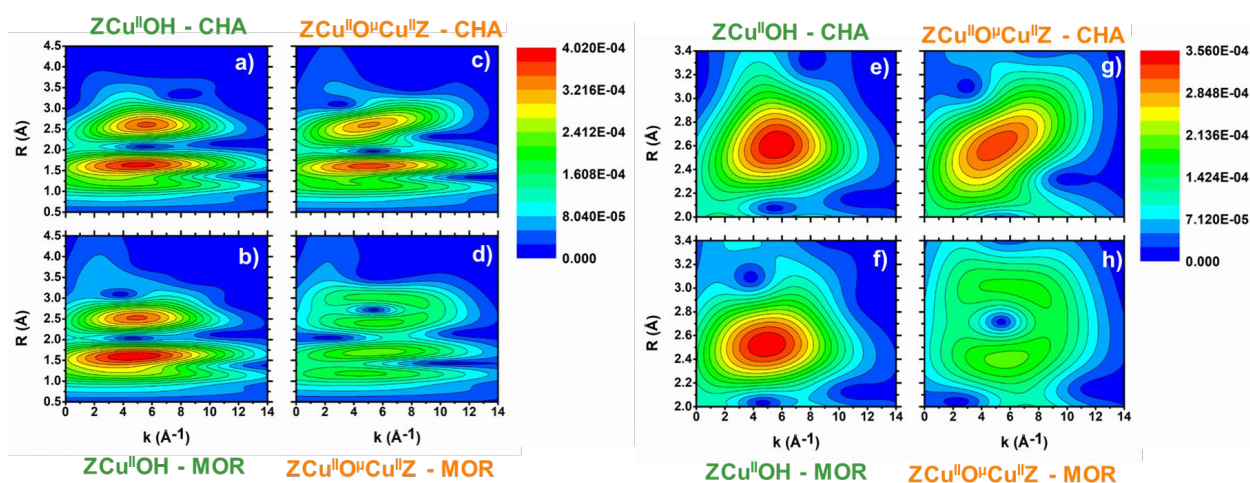

Figure 5. (a-d) Full-range EXAFS WT 2D plots for monomeric ZCu^{II}OH and dimeric ZCu^{II}O$^{\mu}$Cu^{II}Z species in CHA 8MR, parts (a) and (c), and MOR 12MR, parts (b) and (d). (e-h) Respective magnifications of the second WT lobe located between 2.0 and 3.5 Å, corresponding to the second-shell region in conventional EXAFS-FT.

Analyzing the dimeric ZCu^{II}O$^{\mu}$Cu^{II}Z configurations, more differences appear between the two framework topologies. In CHA framework, the mono-(μ-oxo) dicopper(II) complex is located in the 8MR, while in MOR it lies in the 12MR plane. This implies that in CHA, from the second coordination shell upward, the distances between the Cu absorbers and its atomic neighbors (Al, farer framework Si/O and Cu) are lower than in MOR. Consequently, a higher overlap of the atomic contributions in the 2.0–3.5 Å range is observed for ZCu^{II}O$^{\mu}$Cu^{II}Z in CHA with respect to the same species in MOR, see Figure 4c,d.

The simulated EXAFS-FT spectra for ZCu^{II}O$^{\mu}$Cu^{II}Z and ZCu^{II}OH in the CHA 8MR are almost overlapped (Figure 4e): by standard EXAFS analysis it would be very challenging to discriminate among these mono- and di-copper(II) species. Conversely, for ZCu^{II}O$^{\mu}$Cu^{II}Z in the MOR 12MR, the second-shell peak in the standard EXAFS-FT shows two sub-peaks, whose conformation is more complex if compared to what observed for ZCu^{II}OH in the same framework (Figure 4f). The first sub-shell peak is principally due to the SS contributions from the Al and framework Si/O atoms, while the second one is mostly related to the presence of the framework Si/O atoms and the second Cu site.

A more evident representation comes, in this case, from the WT analysis of the EXAFS signal (Figure 5). At low R values the WT plots show the characteristic structured lobe due to the first-shell O_{fw} and O_{efw} contributions, broadened in k-space as discussed before for monomeric $ZCu^{II}OH$ species. However, the second main lobe, extending in the region between $\Delta R = (2.0\text{–}3.5\text{ Å})$ and $\Delta k = (0.5\text{–}12.0\text{ Å}^{-1})$ presents an interesting conformation. As visible in the magnification reported in Figure 5g,h, it is clearly composed by the combination of two sub-lobes. The first one, in the $\Delta k = (0.5\text{–}6.0\text{ Å}^{-1})$, stems from the contributions of Al and farer framework Si/O and atoms, whose backscattering amplitude factor peaks in the k-space around 3-4 Å^{-1} (Figure 1). The second sub-lobe extends in the $\Delta k = (6.0\text{–}12.0\text{ Å}^{-1})$ range. The maximum of the Cu backscattering amplitude falls exactly within this k-space region, allowing an unambiguous assignment of this sub-lobe to Cu–Cu contributions.

Standard EXAFS-FT analysis highlights how for $ZCu^{II}O^{\mu}Cu^{II}Z$ in the CHA 8MR the Si/O framework contributions overlap with the Cu–Cu one in the same R space range (Figure 4d). The Si SS paths are characterized by a backscattering amplitude factor that is lower in magnitude at high k-values than for Cu, but still not negligible. This is the main reason why the Cu sub-lobe is not completely separated from the sub-lobe collectively stemming from O, Al, and Si scatterers, making its complete resolution impossible to realize for this structural configuration of the dimeric core. Nevertheless, considering the poor contrast between the standard EXAFS-FT spectra simulated for $ZCu^{II}O^{\mu}Cu^{II}Z$ and $ZCu^{II}OH$ in CHA (Figure 4e), it clearly emerges how WTA can, in such case, provide enhanced sensitivity to the nuclearity of the investigated Cu-species.

For $ZCu^{II}O^{\mu}Cu^{II}Z$ in the MOR 12MR, the larger ring size reflects into a better peak resolution in the EXAFS-FT plot, see Figure 4d. Here, the Cu–Cu path is associated to a well-resolved third-shell maximum and its contribution becomes clearly evident in the WT representation, where a lobe extends in the region included between $\Delta R = (2.7\text{–}3.4\text{ Å})$ and $\Delta k = (6.0\text{–}12.0\text{ Å}^{-1})$, characteristic of Cu (Figure 5 d,h).

3.4 Critical comparison between theoretical and experimental XAS results

In the previous Sections, we have examined by computational modelling and DFT-assisted simulations the characteristic XANES and EXAFS features for well-defined Cu^{II}-oxo species in the CHA and MOR frameworks. In the following, we will critically compare these theoretical findings with representative experimental results. With this respect, Figure 6 reports a selection of previously published [32] experimental XAS spectra of O_2-activated Cu-CHA and Cu-MOR, with similar compositional characteristics and measured after identical activation protocols.

In line with simulations reported in Section 3.2, Cu-MOR and Cu-CHA show very similar Cu K-edge XANES spectra. The experimental XANES, characteristic of Cu^{II} centers, show a rising-edge peak at ca. 8987 eV and an intense WL peak at ca. 8997 eV, with a shoulder on the low-energy side at ca. 8993 eV. Simulations reasonably reproduced the major experimental XANES features and their energy location. However, the relative intensity of rising-edge peaks with respect to the WL peak is overestimated, especially for three-fold coordinated Cu^{II} moieties.

Taking into account XANES simulations for Cu^{I} and Cu^{II} oxides (see Supplementary Material, Figure S5), one should recall that the full potential FDM approach tends to overestimate the intensity and sharpness of rising-edge feature for $Cu^{II}O$. Assuming a similar behavior for XANES simulation of Cu-oxo species in zeolites, we could explain the difference with the experimental XANES reported in Figure 6a, as well as in other XAS studies [11, 14, 15, 18, 33], where a broader, lower-intensity rising edge peak is detected. Also, different Cu^{II} species have been shown to be simultaneously present in Cu-CHA [10, 11, 64, 68] and Cu-MOR [15, 69] after activation – plausibly involving a

mixture of three- and four-fold coordinated Cu centers. In addition, especially at high temperature, a significant mobility level have been proposed even for framework-coordinated ions [64, 70]. All these factors are expected to contribute to a dampening/broadening effect in the experimental XANES features.
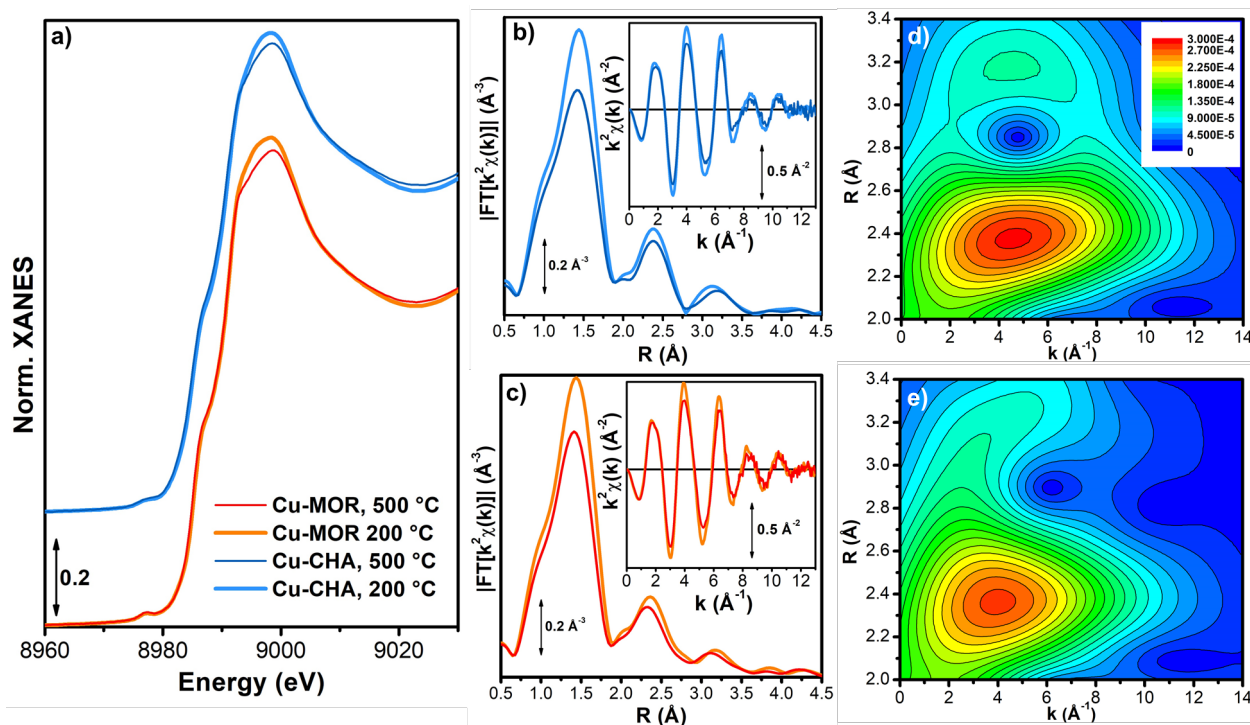

Figure 6. Selection of experimental *in situ* XAS results collected at 500 °C and 200 °C on O_2-activated Cu-CHA and Cu-MOR zeolites. (a) Cu K-edge XANES spectra, vertically translated for the sake of clarity. (b. c) Magnitude of EXAFS-FT spectra for (b) Cu-CHA and (c) Cu-MOR, obtained transforming the $k^2\chi(k)$ curves shown in the respective insets, in the k-range 2.4-11.0 Å^{-1}. (d, e) Experimental EXAFS WT 2D plots for the 200 °C EXAFS spectra reported in part (b, c), chosen for its better S/N ratio in the EXAFS and magnified in the region of the second WT lobe between 2.0 and 3.5 Å. The same ranges in k and R spaces used to compute theoretical WT plots have been adopted also in this case. Unpublished figure, reporting experimental data previously published in ref. [32]

The experimental EXAFS-FT spectra in Figure 6b,c also corroborate the indications by DFT-modelling about the similarity of local environment of Cu-centers in the two investigated zeolites. In both cases, three maxima are observed, at equivalent R-values for the two frameworks. The rather broad first-shell peak contains contributions from O atoms in the first coordination shell of Cu centers. In line with previous EXAFS results for Cu-CHA [11, 18], two Cu−O_{ef} and Cu−O_{fw} sub-shells at slightly different distances (refined e.g. at 1.86 ± 0.05 Å and 1.97 ± 0.04 Å, respectively, in ref. [11]) are required to reach a satisfactory fit of the EXAFS spectra. This asymmetric coordination mode is typically observed in DFT geometries of three-coordinated Cu-species. Nonetheless, it is clear that O_{ef} and O_{fw} contributions in the experimental spectra are more overlapped in R-space with respect to what we observe in the simulated EXAFS spectra in Section 3.3, reflecting larger differences between Cu−O_{ef} and Cu−O_{fw} distances in the DFT models of the three-fold coordinated Cu^{II}-sites. The presence of a fractional contribution from four-fold coordinated Cu^{II}-moieties, predicted to possess very similar Cu−O_{ef} and Cu−O_{fw} distances (e.g. for ZCu^{II}O_2^{side}, Cu-O_{ef} ~ 1.96 Å and Cu-O_{fw} ~ 1.98 Å, see Tables S4, S5) could explain this observation.

It is interesting to observe how, for both Cu-CHA and Cu-MOR, cooling to 200 °C in O_2 results into an appreciable increase in the intensity of the WL peak in the experimental XANES spectra together

with an intensity enhancement of the EXAFS first-shell peak, beside what is expected only due to lower thermal contribution to Debye-Waller factors [11]. In line with the XANES simulations in Section 3.2, such behavior could be connected with an increased relative fraction of four-fold coordinated Cu^{II} moieties, such as $ZCu^{II}O_2^{side}$, at lower temperature.

Based on encouraging results presented in Section 3.3, we have applied WTA to the experimental EXAFS spectra reported in Figure 6b,c. Figure 6d,e reports the resulting EXAFS WT 2D plots, magnified in the 2.0-3.4 Å range. Indeed, interpretation of the experimental signal is more demanding in this region, due to overlapping contributions from different types of atomic neighbors (full-range EXAFS WT plots can be found in the Supplementary Material, Figure S9).

For both Cu-zeolites, we observe lobes extending in the $\Delta k = (6.0–12.0 \text{ Å}^{-1})$ interval, characteristic of Cu−Cu scattering contributions. Thus, WTA supports the presence of an appreciable fraction of multimeric Cu-species in both cases, which would have been difficult to unambiguously assess only from conventional FT-EXAFS spectra in Figure 6b,c. Interestingly, WT plots for Cu-CHA and MOR also show a slightly different morphology. For Cu-CHA, the high-k lobe appears at higher R-values than in Cu-MOR, in the $\Delta R = (2.7–3.0 \text{ Å})$ range − across the second and third maxima observed in the FT-EXAFS spectrum. Conversely, for Cu-MOR, a more pronounced high-k lobe is observed in the $\Delta R = (2.2–2.6 \text{ Å})$ range, corresponding to the second maximum in the FT-EXAFS spectrum. Although a detailed analysis of these results is beyond the scope of the present work, we could envisage Cu-dimers with larger average Cu−Cu separation (possibly $ZCu^{II}O_2^{end}Cu^{II}Z$ peroxides) to form in the Cu-CHA sample with respect to Cu-MOR.

4. Conclusions and perspectives

In the present work we have explored by theory a number of Cu^{II}-oxo species hosted in the CHA and MOR frameworks, aiming to address limitations and potential of the XAS technique applied to the characterization of O_2-activated Cu-zeolites. Accurate determination of the nuclearity of Cu-species in zeolites represents an ongoing challenge with implications for both MTM and NH_3-SCR reactions [2, 15]. In our endeavor to expand the fundamental knowledge basis required for a robust XAS data interpretation, we have thus simulated and critically compared the XAS features stemming from DFT-optimized geometries for both monomeric and dimeric Cu^{II} moieties in the 8MR and 12MR of CHA and MOR, respectively.

Our computational screening, in line with previous theoretical reports [51, 52], highlighted how the first-shell environment of Cu ions (O_{fw} atoms from the zeolite lattice and extra-framework O_{ef} from OH and active oxygen ligands) is rather insensitive to the zeolite topology and to the framework location. Conversely, from the second-shell upward, appreciable differences are noted, translating *e.g.* in longer Cu–Al and Cu–Cu distances for dicopper(II) species in the larger MOR 12MR ring with respect to the CHA 8MR.

Cu K-edge XANES simulations indicated that XANES is mostly sensitive to the first-shell coordination geometry, providing sufficient spectroscopic contrast among four-fold and three-fold coordinated Cu^{II} centers. Conversely, it lacks specific sensitivity to the nuclearity of Cu-species, so that monomers and dimers retaining the same three-fold coordination mode result into very similar XANES spectra.

EXAFS is a well-established technique to accurately determine the local structure around dispersed metal centers [2, 29]. However, when the standard EXAFS-FT approach is applied to these specific systems, it also encounters difficulties, mostly due to the co-localization in the second-shell R-space

range of scattering contributions from different types of atomic neighbors, including O, Al, Si and Cu atoms. The reported simulated EXAFS-FT spectra for the DFT-optimized geometries of two representative mono- and di-copper(II) species, namely $ZCu^{II}O^{\mu}Cu^{II}Z$ and $ZCu^{II}OH$, well exemplify this issue.

With this respect, we also explored the potential of EXAFS Wavelet Transform Analysis (WTA) [34-38], computing the theoretical WT 2D-maps for the same monomeric and dimeric species in the CHA and MOR zeolites. For $ZCu^{II}O^{\mu}Cu^{II}Z$ dimers, specific features unambiguously assigned to Cu–Cu scattering contribution arise in the high-k range of the WT plane, which are absent in the case of $ZCu^{II}OH$ monomers. Based on these findings, WTA is envisaged as a valid complement to conventional EXAFS-FT approach, to unravel the elusive contributions from Cu-oxo dimers, and in general small metal-oxo clusters, stabilized into zeolitic lattices upon high-temperature oxidative treatment.

Finally, we have critically compared the results of our theoretical screening with representative experimental XANES and EXAFS spectra for O_2-activated Cu-CHA and Cu-MOR. The simulated XAS response from atomically-defined Cu^{II}-oxo species is effective in guiding the interpretation of experimental data on Cu-zeolites. WTA applied to experimental EXAFS spectra appears to represent a promising tool to resolve the presence of multimeric Cu-species. However, open challenges in this context remain, mostly in connection with (i) the simultaneous presence of multiple Cu^{II} species/sites under the typical synthesis/pretreatment conditions and (ii) the temperature-dependent dynamics involving each Cu-species, in terms of mobility of Cu-ions around the most stable configurations and possible temperature-dependent interconversion phenomena. Future perspectives to further progress in the field will consider advanced modelling strategies, such as molecular dynamics-based XANES and EXAFS simulations, similarly to what has been recently reported by Li et al. for UV-Vis spectra [64]. In parallel, we could envisage *ad hoc* synthesis [61, 62] and/or pretreatment protocols [15] promoting "single-site" scenarios, as well as statistical analysis of large XAS data series [15, 19, 68] to isolate the spectroscopic signatures and concentration profiles of individual Cu-species.

References

[1]   B. Smit, T.L.M. Maesen, Nature 451 (2008) 671-678.
[2]   E. Borfecchia, P. Beato, S. Svelle, U. Olsbye, C. Lamberti, S. Bordiga, Chem. Soc. Rev. 47 (2018) 8097-8133.
[3]   U. Deka, I. Lezcano-Gonzalez, B.M. Weckhuysen, A.M. Beale, ACS Catal. 3 (2013) 413-427.
[4]   A.M. Beale, F. Gao, I. Lezcano-Gonzalez, C.H.F. Peden, J. Szanyi, Chem. Soc. Rev. 44 (2015) 7371-7405.
[5]   M.J. Wulfers, S. Teketel, B. Ipek, R.F. Lobo, Chem. Commun. 51 (2015) 4447-4450.
[6]   M. Ravi, M. Ranocchiari, J.A. van Bokhoven, Angew. Chem. Int. Ed. 56 (2017) 16464-16483.

[7]   M. Ravi, V.L. Sushkevich, A.J. Knorpp, M.A. Newton, D. Palagin, A.B. Pinar, M. Ranocchiari, J.A. van Bokhoven, Nat. Catal. 2 (2019) 485-494.

[8]   K.T. Dinh, M.M. Sullivan, P. Serna, R.J. Meyer, M. Dincă, Y. Román-Leshkov, ACS Catal. 8 (2018) 8306-8313.

[9]   B.E.R. Snyder, M.L. Bols, R.A. Schoonheydt, B.F. Sels, E.I. Solomon, Chem. Rev. 118 (2018) 2718-2768.

[10]   B. Ipek, M.J. Wulfers, H. Kim, F. Goltl, I. Hermans, J.P. Smith, K.S. Booksh, C.M. Brown, R.F. Lobo, ACS Catal. 7 (2017) 4291-4303.

[11]   D.K. Pappas, E. Borfecchia, M. Dyballa, I.A. Pankin, K.A. Lomachenko, A. Martini, M. Signorile, S. Teketel, B. Arstad, G. Berlier, C. Lamberti, S. Bordiga, U. Olsbye, K.P. Lillerud, S. Svelle, P. Beato, J. Am. Chem. Soc. 139 (2017) 14961–14975.

[12]   E.M.C. Alayon, M. Nachtegaal, A. Bodi, J.A. van Bokhoven, ACS Catal. 4 (2014) 16-22.

[13]   V.L. Sushkevich, D. Palagin, M. Ranocchiari, J.A. van Bokhoven, Science 356 (2017) 523-527.

[14]   S. Grundner, M.A.C. Markovits, G. Li, M. Tromp, E.A. Pidko, E.J.M. Hensen, A. Jentys, M. Sanchez-Sanchez, J.A. Lercher, Nat. Commun. 6 (2015) 9.

[15]   D.K. Pappas, A. Martini, M. Dyballa, K. Kvande, S. Teketel, K.A. Lomachenko, R. Baran, P. Glatzel, B. Arstad, G. Berlier, C. Lamberti, S. Bordiga, U. Olsbye, S. Svelle, P. Beato, E. Borfecchia, J. Am. Chem. Soc. 140 (2018) 15270-15278.

[16]   K.A. Lomachenko, E. Borfecchia, C. Negri, G. Berlier, C. Lamberti, P. Beato, H. Falsig, S. Bordiga, J. Am. Chem. Soc. 138 (2016) 12025-12028.

[17]   M.H. Groothaert, P.J. Smeets, B.F. Sels, P.A. Jacobs, R.A. Schoonheydt, J. Am. Chem. Soc. 127 (2005) 1394-1395.

[18]   E. Borfecchia, K.A. Lomachenko, F. Giordanino, H. Falsig, P. Beato, A.V. Soldatov, S. Bordiga, C. Lamberti, Chem. Sci. 6 (2015) 548-563.

[19]   A. Martini, E. Borfecchia, K.A. Lomachenko, I.A. Pankin, C. Negri, G. Berlier, P. Beato, H. Falsig, S. Bordiga, C. Lamberti, Chem. Sci. 8 (2017) 6836-6851.

[20]   C. Paolucci, I. Khurana, A.A. Parekh, S. Li, A.J. Shih, H. Li, J.R. Di Iorio, J.D. Albarracin-Caballero, A. Yezerets, J.T. Miller, W.N. Delgass, F.H. Ribeiro, W.F. Schneider, R. Gounder, Science 357 (2017) 898-903.

[21]   A. Marberger, A.W. Petrov, P. Steiger, M. Elsener, O. Kröcher, M. Nachtegaal, D. Ferri, Nat. Catal. 1 (2018) 221-227.

[22]   A.G. Greenaway, I. Lezcano-Gonzalez, M. Agote-Aran, E.K. Gibson, Y. Odarchenko, A.M. Beale, Top. Catal. 61 (2018) 175-182.

[23]   A.R. Fahami, T. Günter, D.E. Doronkin, M. Casapu, D. Zengel, T.H. Vuong, M. Simon, F. Breher, A.V. Kucherov, A. Brückner, J.D. Grunwaldt, React. Chem. Eng. 4 (2019) 1000-1018.

[24]   K.A. Lomachenko, A. Martini, D.K. Pappas, C. Negri, M. Dyballa, G. Berlier, S. Bordiga, C. Lamberti, U. Olsbye, S. Svelle, P. Beato, E. Borfecchia, Catal. Today 336 (2019) 99-108.

[25]   T.V.W. Janssens, H. Falsig, L.F. Lundegaard, P.N.R. Vennestrøm, S.B. Rasmussen, P.G. Moses, F. Giordanino, E. Borfecchia, K.A. Lomachenko, C. Lamberti, S. Bordiga, A. Godiksen, S. Mossin, P. Beato, ACS Catal. 5 (2015) 2832-2845.

[26]   I. Lezcano-Gonzalez, D.S. Wragg, W.A. Slawinski, K. Hemelsoet, A. Van Yperen-De Deyne, M. Waroquier, V. Van Speybroeck, A.M. Beale, J. Phys. Chem. C 119 (2015) 24393-24403.

[27]   E. Borfecchia, C. Negri, K.A. Lomachenko, C. Lamberti, T.V.W. Janssens, G. Berlier, React. Chem. Eng. 4 (2019) 1067-1080.

[28]   C. Negri, E. Borfecchia, M. Cutini, K.A. Lomachenko, T.V.W. Janssens, G. Berlier, S. Bordiga, ChemCatChem 11 (2019) 3828-3838.

[29]   S. Bordiga, E. Groppo, G. Agostini, J.A. van Bokhoven, C. Lamberti, Chem. Rev. 113 (2013) 1736-1850.

[30]   L. Mino, G. Agostini, E. Borfecchia, D. Gianolio, A. Piovano, E. Gallo, C. Lamberti, J. Phys. D-Appl. Phys. 46 (2013) 72.

[31]   K.A. Lomachenko, E. Borfecchia, S. Bordiga, A.V. Soldatov, P. Beato, C. Lamberti, J. Phys.: Conf. Ser. 712 (2016) 012041.

[32]   E. Borfecchia, D.K. Pappas, M. Dyballa, K.A. Lomachenko, C. Negri, M. Signorile, G. Berlier, Catal. Today 333 (2019) 17-27.

[33] C. Paolucci, A.A. Parekh, I. Khurana, J.R. Di Iorio, H. Li, J.D.A. Caballero, A.J. Shih, T. Anggara, W.N. Delgass, J.T. Miller, F.H. Ribeiro, R. Gounder, W.F. Schneider, J. Am. Chem. Soc. 138 (2016) 6028-6048.
[34] M. Munoz, P. Argoul, F. Farges, Am. Miner. 88 (2003) 694-700.
[35] H. Funke, A.C. Scheinost, M. Chukalina, Phys. Rev. B 71 (2005) 7.
[36] J. Timoshenko, A. Kuzmin, Comput. Phys. Commun. 180 (2009) 920-925.
[37] T.J. Penfold, I. Tavernelli, C.J. Milne, M. Reinhard, A. El Nahhas, R. Abela, U. Rothlisberger, M. Chergui, J. Chem. Phys. 138 (2013) 7.
[38] M.A. Soldatov, A. Martini, A.L. Bugaev, I. Pankin, P.V. Medvedev, A.A. Guda, A.M. Aboraia, Y.S. Podkovyrina, A.P. Budnyk, A.A. Soldatov, C. Lamberti, Polyhedron 155 (2018) 232-253.
[39] G. Kresse, J. Furthmuller, Comput. Mater. Sci. 6 (1996) 15-50.
[40] J.P. Perdew, K. Burke, M. Ernzerhof, Phys. Rev. Lett. 77 (1996) 3865-3868.
[41] S. Grimme, J. Antony, S. Ehrlich, H. Krieg, J. Chem. Phys. 132 (2010) 19.
[42] A.V. Krukau, O.A. Vydrov, A.F. Izmaylov, G.E. Scuseria, J. Chem. Phys. 125 (2006) 224106.
[43] Y. Joly, Phys. Rev. B 63 (2001) 10.
[44] Y. Joly, S. Di Matteo, C.R. Natoli, Phys. Rev. B 69 (2004) 11.
[45] L. Hedin, B.I. Lundqvist, J. Phys. C Solid State Phys. 4 (1971) 2064.
[46] S.A. Guda, A.A. Guda, M.A. Soldatov, K.A. Lomachenko, A.L. Bugaev, C. Lamberti, W. Gawelda, C. Bressler, G. Smolentsev, A.V. Soldatov, Y. Joly, J. Chem. Theory Comput. 11 (2015) 4512-4521.
[47] M.O. Krause, J.H. Oliver, J. Phys. Chem. Ref. Data 8 (1979) 329-338.
[48] B. Ravel, M. Newville, J. Synchrotron Radiat. 12 (2005) 537-541.
[49] E. Sevillano, H. Meuth, J.J. Rehr, Phys. Rev. B 20 (1979) 4908-4911.
[50] S. Nikitenko, A.M. Beale, A.M.J. van der Eerden, S.D.M. Jacques, O. Leynaud, M.G. O'Brien, D. Detollenaere, R. Kaptein, B.M. Weckhuysen, W. Bras, J. Synchrotron Rad. 15 (2008) 632-640.
[51] L. Vilella, F. Studt, Eur. J. Inorg. Chem. (2016) 1514-1520.
[52] H. Falsig, P.N.R. Vennestrom, P.G. Moses, T.V.W. Janssens, Top. Catal. 59 (2016) 861-865.
[53] F. Giordanino, P.N.R. Vennestrom, L.F. Lundegaard, F.N. Stappen, S. Mossin, P. Beato, S. Bordiga, C. Lamberti, Dalton Trans. 42 (2013) 12741-12761.
[54] P. Vanelderen, B.E.R. Snyder, M.-L. Tsai, R.G. Hadt, J. Vancauwenbergh, O. Coussens, R.A. Schoonheydt, B.F. Sels, E.I. Solomon, J. Am. Chem. Soc. 137 (2015) 6383-6392.
[55] E.M. Alayon, M. Nachtegaal, A. Bodi, M. Ranocchiari, J.A. van Bokhoven, Phys. Chem. Chem. Phys. 17 (2015) 7681-7693.
[56] P.J. Smeets, R.G. Hadt, J.S. Woertink, P. Vanelderen, R.A. Schoonheydt, B.F. Sels, E.I. Solomon, J. Am. Chem. Soc. 132 (2010) 14736-14738.
[57] E.I. Solomon, D.E. Heppner, E.M. Johnston, J.W. Ginsbach, J. Cirera, M. Qayyum, M.T. Kieber-Emmons, C.H. Kjaergaard, R.G. Hadt, L. Tian, Chem. Rev. 114 (2014) 3659-3853.
[58] J.L. DuBois, P. Mukherjee, A.M. Collier, J.M. Mayer, E.I. Solomon, B. Hedman, T.D.P. Stack, K.O. Hodgson, J. Am. Chem. Soc. 119 (1997) 8578-8579.
[59] S. Sklenak, J. Dědeček, C. Li, B. Wichterlová, V. Gábová, M. Sierka, J. Sauer, Phys. Chem. Chem. Phys. 11 (2009) 1237-1247.
[60] O.H. Han, C.-S. Kim, S.B. Hong, Angew. Chem. Int. Edit. 41 (2002) 469-472.
[61] J.R. Di Iorio, R. Gounder, Chem. Mater. 28 (2016) 2236-2247.
[62] J.R. Di Iorio, C.T. Nimlos, R. Gounder, ACS Catal. 7 (2017) 6663-6674.
[63] J.S. McEwen, T. Anggara, W.F. Schneider, V.F. Kispersky, J.T. Miller, W.N. Delgass, F.H. Ribeiro, Catal. Today 184 (2012) 129-144.
[64] H. Li, C. Paolucci, I. Khurana, Laura N. Wilcox, F. Göltl, J.D. Albarracin-Caballero, A.J. Shih, F.H. Ribeiro, R. Gounder, W.F. Schneider, Chem. Sci. 10 (2019) 2373-2384.
[65] R. Zhang, J.-S. McEwen, J. Phys. Chem. Lett. 9 (2018) 3035-3042.
[66] S.J. Clark, M.D. Segall, C.J. Pickard, P.J. Hasnip, M.J. Probert, K. Refson, M.C. Payne, Z. Kristallogr. 220 (2005) 567-570.
[67] U. Deka, A. Juhin, E.A. Eilertsen, H. Emerich, M.A. Green, S.T. Korhonen, B.M. Weckhuysen, A.M. Beale, J. Phys. Chem. C 116 (2012) 4809-4818.
[68] A. Martini, E. Alladio, E. Borfecchia, Top. Catal. 61 (2018) 1396-1407.
[69] V.L. Sushkevich, D. Palagin, J.A. van Bokhoven, Angew. Chem. Int. Ed. 57 (2018) 8906-8910.
[70] F. Göltl, P. Sautet, I. Hermans, Catal. Today 267 (2016) 41-46.